SCIENCE CHINA
Chemistry

•ARTICLES•

July 2022 Vol.65 No.7: 1306–1314
https://doi.org/10.1007/s11426-022-1230-x

Maillard reaction-derived laser lithography for printing functional inorganics

Xiao Dai[1,2†], Yining Jiang[1†], Xiaohan Wang[3], Fengnan Chen[1], Liang Gao[1], Xiaofeng Li[1] & Guifu Zou[1*]

[1]*School of Energy, School of Optoelectronic Science and Engineering, Key Laboratory of Advanced Carbon Materials and Wearable Energy Technologies of Jiangsu Province, Soochow University, Suzhou 215006, China;*
[2]*School of Optical and Electronic Information, Suzhou City University, Suzhou 215104, China;*
[3]*Research Institute of Superconductor Electronics, College of Engineering and Applied Science, Nanjing University, Nanjing 210023, China*

Received January 12, 2022; accepted March 21, 2022; published online May 26, 2022

Photopolymerization-based additive printing of functional inorganics has drawn great attention in recent years and one important challenge is the photoresin loading with diverse inorganics. Here, we introduce a Maillard reaction-derived laser lithography strategy for an unprecedented direct printing of diverse inorganic compounds. The sugar-assisted laser lithography (SLL) is powerful to carry choice metal ions and versatile for the generation of patterned inorganic materials comprising metal oxides, metal sulfides, and metal nitrides, characterized by ferroelectric, magnetic, semiconductivity, superconductivity, or other properties. The material architecture is flexibly manipulated by the laser intensity, power, printing speed, precursor solution, and computer-aided design to satisfy the practical requirements. This work demonstrates a new possibility for the further development of laser lithography in the directly printing of feature-rich inorganic materials and devices.

functional inorganics, inorganic nanomaterials, printing nanostructures

Citation: Dai X, Jiang Y, Wang X, Chen F, Gao L, Li X, Zou G. Maillard reaction-derived laser lithography for printing functional inorganics. *Sci China Chem*, 2022, 65: 1306–1314, https://doi.org/10.1007/s11426-022-1230-x

1 Introduction

The photolithography of functional inorganic thin films is the basis of the information technique industry that fabricates chips and integrated circuits. Conventional planar photolithography can pattern inorganic thin films through subtractive procedures, which involve film deposition, photoresin coating, exposition, development, wet or dry etching, and resist stripping. In recent years, the development of photopolymerization-based additive printing of inorganics has drawn great attention [1–4]. In this new method, inorganic precursors are loaded in the photoresin and designed 2D or 3D geometries of inorganics are produced by photoshaping and post treatment processes. Compared with conventional subtractive photolithography, the additive printing route is much simplified and more adapted to customized applications of micromachines [1], photonics [2], electronics [3], and chemistry and biology [4]. However, one of the most important challenges is to develop photoresins that are able to carry various functional inorganics. Important contributions have shown how to integrate inorganics and precursors of inorganics into photoresins and how to perform additive printing. The precursors can be classified into three families that include metal salts, metal-organics, and nanoparticles. Metal salts such as $HAuCl_4$ and $AgNO_3$ were directly mixed with the photoresin [5,6] and the metal ions were reduced *in situ* to metal nanoparticles by two-photon lithography during

†These authors contributed equally to this work.
*Corresponding author (email: zouguifu@suda.edu.cn)

the resist shaping process, but only a hybrid nanoparticles-polymer matrix was printed due to the low loading ratio. Metal-organic precursors such as nickel acrylate [7], titanium acrylate [8], and organosilicon compounds have been mixed with the photoresin and printed into designed structures [9,10], producing pure phase geometries of metals or ceramics by the pyrolysis process that decomposes the polymer. However, the category of photoresin-compatible metal-organics is still limited and only a few types of inorganics could be printed through this route. Nanoparticles of lead zirconate titanate [3], silica [11], hydroxyapatite [12], zirconia [13], and alumina [14] have been physically blended with the photoresin or chemically bonded with photo-active monomers for additive printing, but the nanoparticle size must be highly uniform and the nanoparticle aggregation and light scattering effects tend to reduce the printing accuracy and uniformity. Furthermore, new strategies have been constantly reported for delivering and printing inorganics, such as metal-silk composites by the lithography of silk-centered bio-resists [15], or direct lithography of colloidal nanocrystals by a photoresin-free method [16], or metal oxides based on an aqueous metal-ion-containing photoresin [17].

The direct laser-writing technology is favorable for nano/microscale additive manufacturing due to its high resolution and facility for printing designed 2D or 3D structures. The additive printing of nano/microstructured inorganics by laser lithography of the above-discussed photosensitive precursors has been studied intensively [3,5–17]. Besides the laser-driven photochemical reaction strategy, another prominent method that is based on the laser sintering of nanoparticle inks has been utilized to print diverse inorganics. Metal nanoparticle inks of gold [18–20], silver [21,22], copper [23,24], and nickel [25–27] have been utilized to print 2D microstructured inorganics and functional devices, including flexible sensors [19], transparent and conductive metal grid electrods [21], wearable sensors [22], transparent heaters [25], and temperature sensors [26]. Nevertheless, the reported routes are still mainly based on specific photoactive preceramic polymers and on nanoparticles that are obtained *via* complex synthetic processes. Researches have been focused on the resolution limit, mechanical strength, conductivity or other basic properties of the printed inorganics. Innovative strategies are still desired for printing more diverse inorganics to enrich printable material sources and endow the additive manufactured inorganics with improved physical, electrical, optical, chemical, and other important properties.

Herein, we develop a sugar-assisted laser lithography (SLL) method that exhibits promising compatibility for carrying diverse metal ions and printing various functional inorganics. The SLL is based on an aqueous solution of maltose and polyethyleneimine (PEI) and the precursor curing mechanism is different from that of the conventional photolithography. It is inspired by the Maillard reaction, which is one of the most important reactions in food chemistry, where a copolymerization of reducing sugars and amino acids occurs [28–30]. The known reaction mechanism at the initial stage involves the condensation of the sugar carbonyl function of the open-chain form with the amino groups of the amino acid [31,32]. In this work, we replace the amino acid with polyethyleneimine (PEI), which is not only rich in amino groups but also a powerful chelating agent for metal ions in aqueous solutions [33,34]. It is found that the sugar and PEI rapidly copolymerize and yield a water-insoluble film upon heating to a threshold temperature. The SLL route is performed by applying a near-infrared (NIR) laser to scan and harden the aqueous precursor and form designed digital micro-patterns on the substrate. Most importantly, using the desired metal ions coordinated to PEI and the SLL processing method, diverse inorganics including metal oxides, metal sulfides, and metal nitrides have been printed on the substrate. The as-patterned inorganic materials were evaluated by functional tests for semiconductivity, superconductivity, magnetic and ferroelectric properties.

2 Methods

For printing ZnO, the precursor was prepared by dissolving 2.5 g of zinc nitrate hexahydrate and 2 g polyethyleneimine in 20 mL of water. After stirring for 1 h, the solution was diluted to 200 mL, subjected to an ultrafiltration process and concentrated to 20 mL. In the ultrafiltration process, an amino ultrafiltration unit and a PM10 ultrafiltration membrane were used. 12 g of maltose was finally added to the solution to form the precursor for performing the SLL procedure. The precursor was spin-coated on substrates at 8,000 r/min for 30 s. The SLL was performed by utilizing a commercial MOPA optical fiber pulsed laser (YDFLO-20-M1, JPT Electronics). The system had the following specifications: laser peak emission wavelength 1,064±15 nm, maximum pulse energy 0.8 mJ, pulse duration adjustable range 2–350 ns, pulse repetition rate adjustable range 1–4,000 kHz, collimated output beam diameter 7 mm, a beam expander 2× (BE-1064-D28:42.4-2X, Carman Haas), a filed lens (SL-1064-175-254, Carman Haas), and a laser scanning galvanometer system. The average output power P is adjustable from 0 to 20 W. For performing SLL in this work, the laser pulse duration τ was set to 40 ns, the pulse repetition rate R was set to 38 kHz, and the laser intensity I was adjusted from 0 to 0.82 TW/cm^2, where I is calculated by the laser parameters [35]. After being scanned by the laser system, the precursor thin film was rinsed with deionized water for 10 s to remove the uncured part, and then the printed patterns on substrate were obtained. Then, the samples were

annealed in air at 400 °C for 60 min and at 600 °C for 30 min, and thus the printed ZnO thin film pattern was obtained for characterization. Other information about the materials, the characterization, and the preparation of the Ni, Sn, Cu, Mo, Ga, Nb, Ba, Ti, and Fe solutions is included in the Supporting Information online, as well as for printing thin films of NiO, SnO, GaN, TiN, MoS_2, CZTS, NbN, $BaTiO_3$ and Ni-Zn ferrite.

3 Results and discussion

The thermally induced copolymerization of PEI with the maltose disaccharide is the basis of SLL. As the precursor thin film is spin-coated on a quartz substrate and heated up at room temperature (Figure 1a), the colorless solid precursor thin film turned brown after 90 °C and was still water resoluble, but subsequently did not redissolve in water, by heating above 120 °C. Monitoring by ultraviolet (UV)-visible spectroscopy (Figure 1b) shows a protruding absorption band centered at ~320 nm after reaching 90 °C, which then vanishes underneath a growing broad absorption band in the 300–450 nm region after being heated above 120 °C. The corresponding thermogravimetric analyses (TGA, Figure 1c) show that the precursor gradually loses weight from room temperature to 180 °C with a distinct derivative thermogravimetric peak centered at 120 °C. X-ray photoemission spectroscopy (XPS, Figure 1d) reveals a remarkable variation for the N1s band of PEI as a result of the thin film curing. The N atoms of pure PEI mainly exist as secondary amines R_2NH (398.8 eV), while approximately 72% of them are transformed to tertiary amines R_3N (400.0 eV) after the copolymerization [36]. This indicates that most of the secondary amines were dehydrated in the reaction with maltose, forming tertiary amines (Figure 1e). Based on the above analyses and the well-known reaction mechanism of the Maillard reaction [37], it can be concluded that the precursor solubility alteration is based on the dehydration and crosslinking of PEI with maltose and that the precursor curing threshold temperature is ~120 °C.

The SLL is performed by applying a laser (1,064 nm) direct writing system to scan and harden the spin-coated precursor thin film on the substrate (Figure 2a). It should be noted that the NIR absorption of the precursor thin film is rather weak (Figure S1, Supporting Information online). The SLL needs to be performed on substrates that absorb the NIR laser energy and that are able to transfer it well to the precursor thin film. Although the Si substrate is almost transparent to ordinary NIR radiation, it has been proven that an intense NIR laser light can be absorbed by Si substrates, generating enough thermal energy [38–40]. In this work, SLL has been successfully accomplished on standard sub-

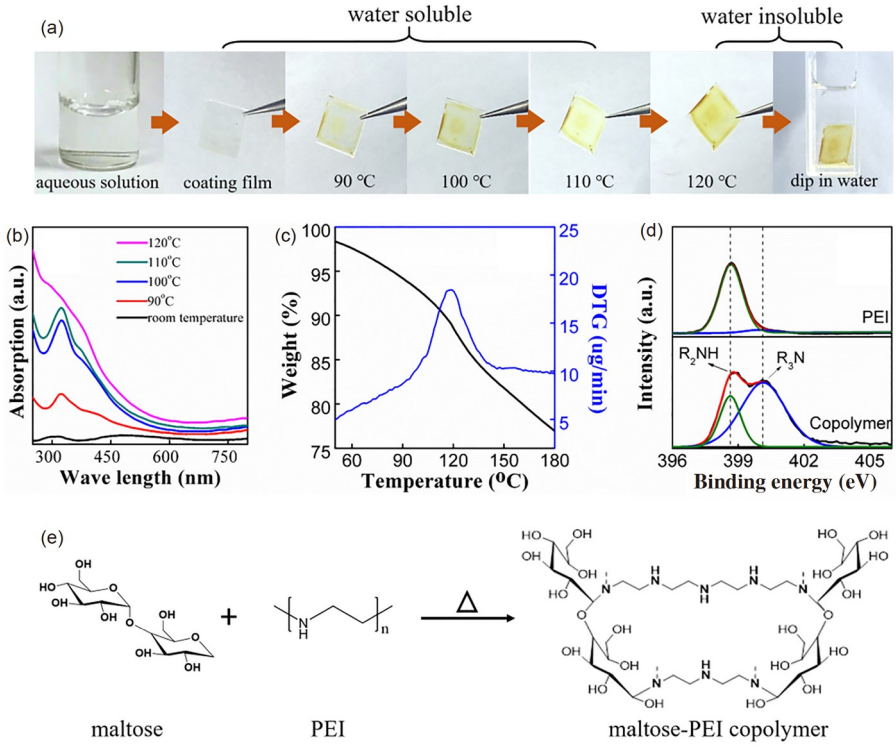

Figure 1 Thermal induced copolymerization of PEI with maltose. (a) Water solubility variation of spin-coated precursor thin film under thermal treatment; (b) absorption spectra of the precursor heated at different temperatures; (c) thermal gravimetric analysis of the precursor; (d) N 1s XPS spectra of PEI and the crosslinked polymer (the red curve refers to the fitting of the raw data; and the green and blue curves correspond to the peak values of R_2NH and R_3N, respectively); (e) crosslinking between maltose and PEI (color online).

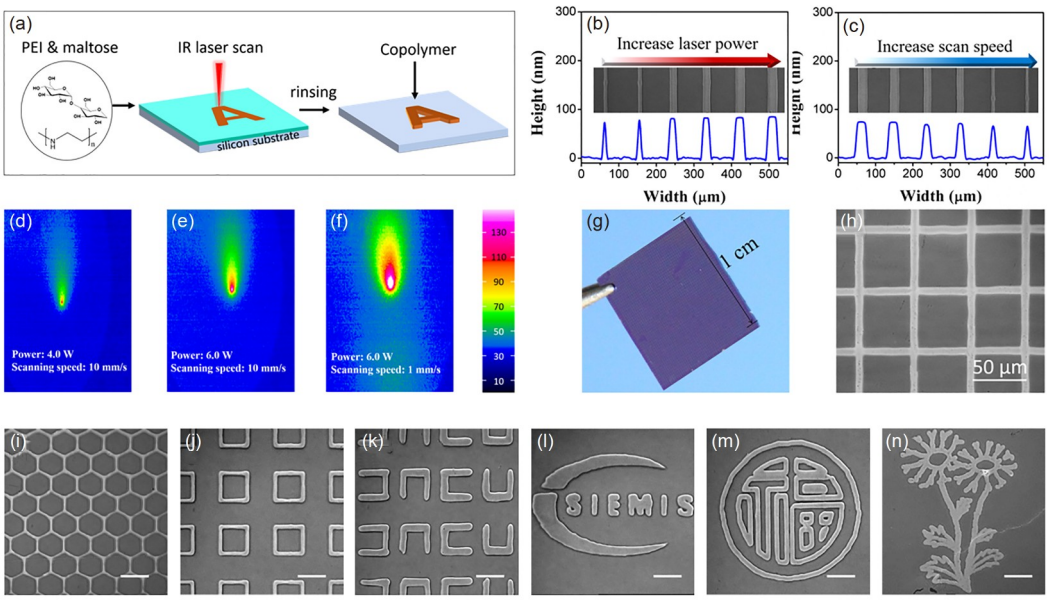

Figure 2 Sugar-assisted laser lithography and the relevant technical features. (a) Illustration of the SSL process; (b) height profile of the patterns printed with different laser output power; (c) height profiles of the patterns printed with different scanning speeds; (d–f) IR images of the laser-induced thermal field on substrates. The laser scanning direction is from top to bottom of the image; (g) picture of a 1 cm × 1 cm substrate printed with grid patterns; (h) microscopic image of the printed pattern in (g) at a printing speed of 1,500 mm/s (scale bar = 50 μm); (i–n) CAD printing of various thin film patterns (scale bar = 100 μm) (color online).

strate materials such as Si, SiO_2/Si, and Ge (Figure S2). The NIR laser direct writing system has a constant beam size of 10 μm, and the influence of the laser working parameters on the printing quality and the size of the printed features was investigated. We found that the printed feature size is tunable by adjusting the laser output power or the laser scan speed, as shown in Figure 2b, c. The feature size increased from 10 to 50 μm when the laser intensity was increased from 0.18 to 0.22 TW/cm^2 at a scanning speed of 5 mm/s. On the other hand, at a constant laser intensity of 0.20 TW/cm^2, the feature size decreased from 40 to 10 μm as the scanning speed was increased from 1 to 25 mm/s. The tuning of the printed feature size was revealed by IR imaging of the laser scanning on a Si substrate (Figure 2d–f). It is observed that the laser output power and the scan speed determine the size of the hot spot on the substrate, which corresponds to the precursor curing zone and determines the printing feature size (Figure S3). As there is a curing threshold temperature, as discussed in Figure 1, the hot spot needs to exceed the curing threshold temperature to induce the precursor curing (Figure S3). Therefore, the laser working parameters (laser output power and scanning speed) need to be finely adjusted within a well-defined functional zone to conduct the SLL (Figure S4). To probe the SLL working limitation, a maximum printing speed of 1,500 mm/s has been demonstrated in this work. A 1 cm × 1 cm substrate (Figure 2g) could be printed with a grid period of 50 μm (Figure 2h) within 5 s. Besides, with the assistance of computer-aided design (CAD), the precursor thin film could be printed with designed digital patterns (Figure 2i–n) and the layer-by-layer structures could also be fabricated through repeating the spin coating and SLL process (Figure S5).

Printing functional inorganics was realized by first coordinating metal ions to the precursor PEI, followed by the SLL process (Figure 3a). Herein, printed ZnO thin film patterns on Si substrates are used as an example for illustration. Zinc nitrate ($Zn(NO_3)_2$) was used as the Zn source to bind with PEI. Designed patterns of the precursor carrying Zn ions could be still printed on the substrate, indicating that the Zn ions do not impede the precursor crosslinking (Figure 3b–d). The corresponding energy-dispersive X-ray spectroscopy (EDX) mapping reveals that the Zn ions are uniformly dispersed within the precursor thin film patterns (Figure S6a). Subsequent ZnO growth was performed through sintering the as-printed samples in air at 500 °C, where the Zn ions were transformed into ZnO while the crosslinked polymer was pyrolyzed away. The transmission electron microscopy (TEM) image of the initial thin film reveals the disorder and amorphous state of the precursor (Figure 3e). Crystalline lattices emerged in the sample after being annealed at 400 °C (Figure 3f), implicating the incipient formation of ZnO nanocrystals. The blurred selected area electron diffraction (SAED) rings also confirm the partially crystalline nature of the phase. After being annealed at 600 °C, highly crystalline ZnO was formed with bright and sharp SAED rings (Figure 3g and Figure S6b). Following the high-temperature treatment, the height of the resultant pattern decreased from 200 to 20 nm (Figure 3h, i) due to the loss of the polymer. The X-ray diffraction (XRD) spectra reveal that the patterned ZnO is polycrystalline, corre-

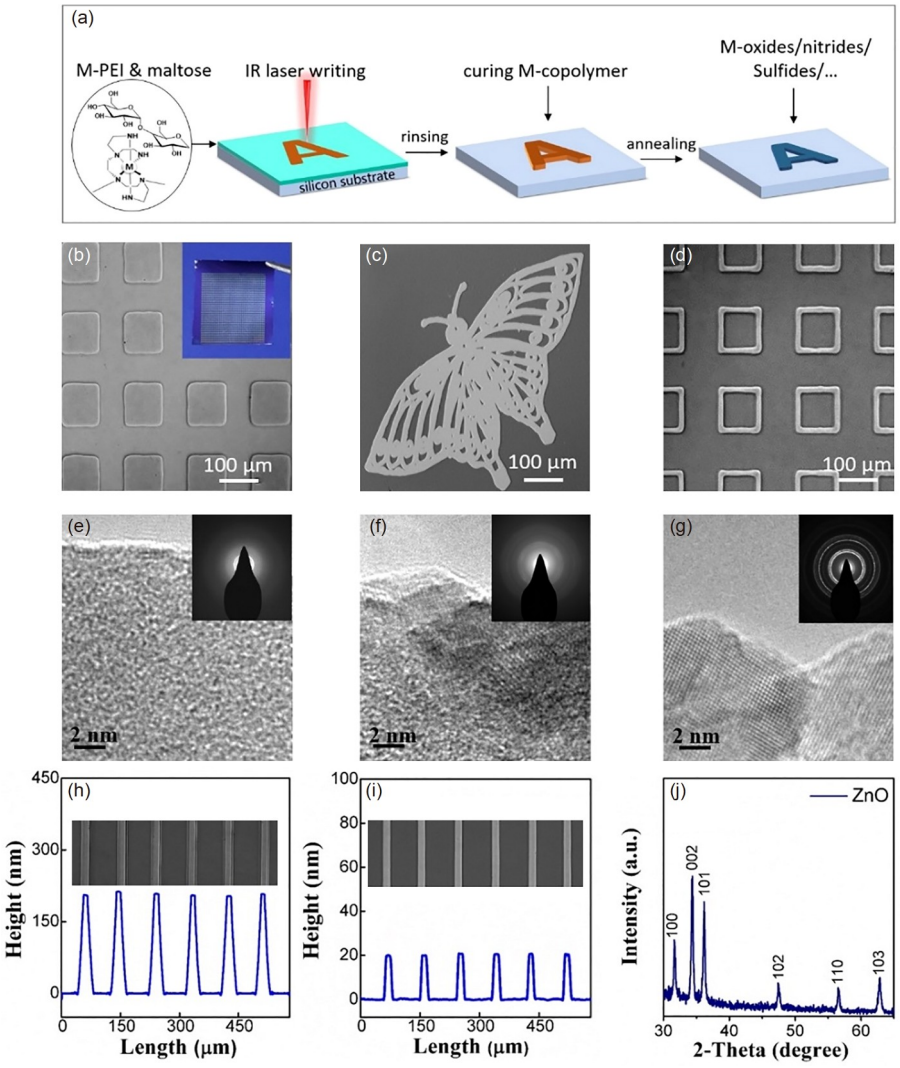

Figure 3 SLL printing of a ZnO thin film. (a) Illustration of the SLL process for printing of inorganics. (b) Microscope image of the printed precursor arrays. The inset is the corresponding optical image of the 1 cm × 1 cm sample. (c, d) Microscope images of a printed micro-butterfly and a rectangle array. (e–g) TEM images of the patterned ZnO during the annealing process. The insets are the corresponding SAED patterns: (e) before being annealed, (f) annealed at 450 °C, (g) annealed at 600 °C. (h) Height profile of the printed precursor thin film patterns loaded with Zn ions. The inset is the corresponding microscopy image of the printed patterns. (i) Height profile of the printed ZnO patterns after annealing at 600 °C. The inset is the corresponding microscopy image of the printed patterns. (j) XRD spectrum of the printed ZnO (color online).

sponding to a pure zincite phase with hexagonal structure (Figure 3j), which agrees with the ZnO thin films previously synthesized through a solution process [41]. The pure zincite phase is confirmed by the corresponding XPS result (Figure S6c), where all of the apparent peaks can be assigned to zinc and oxygen, and no evident signals from carbon or nitrogen are observed, confirming the complete removal of the polymer matrix through the sintering process at 600 °C.

Other inorganic materials have also been printed to further demonstrate the SLL capability. Metal oxide semiconductors (Figure 4a, b) such as *n*-type SnO_2 and *p*-type NiO were obtained through coordination of molecular Sn and Ni precursors, respectively, to PEI followed by printing and sintering and the measured optical band gaps of 3.5 and ~3.3 eV are consistent with bulk materials [42]. The XRD results confirm that the printed oxide film patterns consist of pure and crystallized SnO_2 and NiO phases, respectively (Figure S7a, b). Printed GaN and TiN patterns (Figure 4c, d) were fabricated through the annealing of the Ga and Ti coordinating SLL precursor thin film patterns under an NH_3 atmosphere. The photoluminescence (PL) peak at 395 nm and the XRD spectrum (Figure S7c) confirm the phase quality of GaN [43]. The XPS and XRD results for TiN are in accordance with the reported data as well (Figure S7d) [44]. Printing of the transition metal sulfide MoS_2 was accomplished by the annealing of the Mo coordinating SLLprecursor thin film patterns under an $S_8/H_2/Ar$ atmosphere (Figure 4e). The Raman frequencies at 383 cm^{-1} (E^1_{2g}) and 405 cm^{-1} (A_{1g}) demonstrate that the printed MoS_2 is multilayered [45]. More complicated quaternary semiconductor

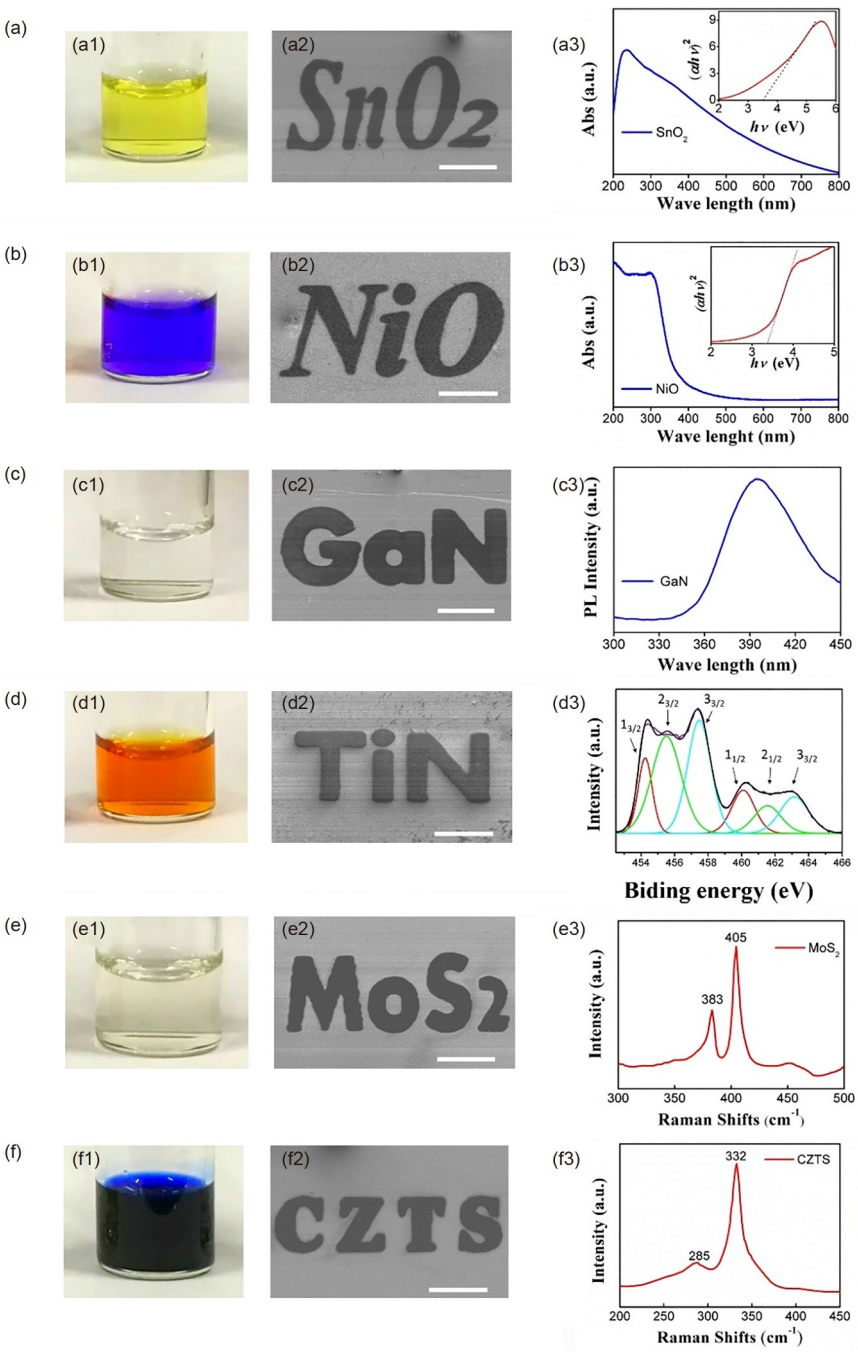

Figure 4 Examples of laser-printed semiconductors. (a1) Sn SLL precursor solution; (a2) SEM image of patterned SnO_2; (a3) UV-Vis spectrum (blue) of SnO_2 and its corresponding band gap (red). (b1) Ni SLL precursor solution; (b2) SEM image of patterned NiO; (b3) UV-Vis spectrum (blue) of NiO and its corresponding band gap (red). (c1) Ga SLL precursor solution; (c2) SEM image of patterned GaN; (c3) PL spectrum of GaN. (d1) Ti SLL precursor solution; (d2) SEM image of patterned TiN; (d3) XPS analysis of the Ti 2p core level. (e1) Mo SLL precursor solution; (e2) SEM image of patterned MoS_2; (e3) Raman spectrum of the obtained MoS_2. (f1) Mixture of SLL precursor of Cu, Zn, and Sn; (f2) SEM image of patterned CZTS; (f3) Raman spectrum of the obtained CZTS. Scale bars = 200 μm in all panels (color online).

copper zinc tin sulfide (CZTS) could also be printed by the incorporation of Cu^{2+}, Zn^{2+}, and Sn^{4+} together into the precursor solution (Figure 4f). The nature and crystallinity of the phase were confirmed by the Raman peaks at 285 and 332 cm^{-1} and by the XRD spectrum (Figure S7e) [46,47].

The quality of the SLL-printed materials was evaluated by the fabrication of functional inorganics as parts of superconductor, magnetic, ferroelectric, and P/N junction devices. Circuitous NbN microwires were printed on a Si substrate (Figure 5a). The cross-section TEM image of the microwire shows that the printed NbN is dense and uniform with a thickness of ~7.1 nm (Figure 5b). The high-resolution TEM

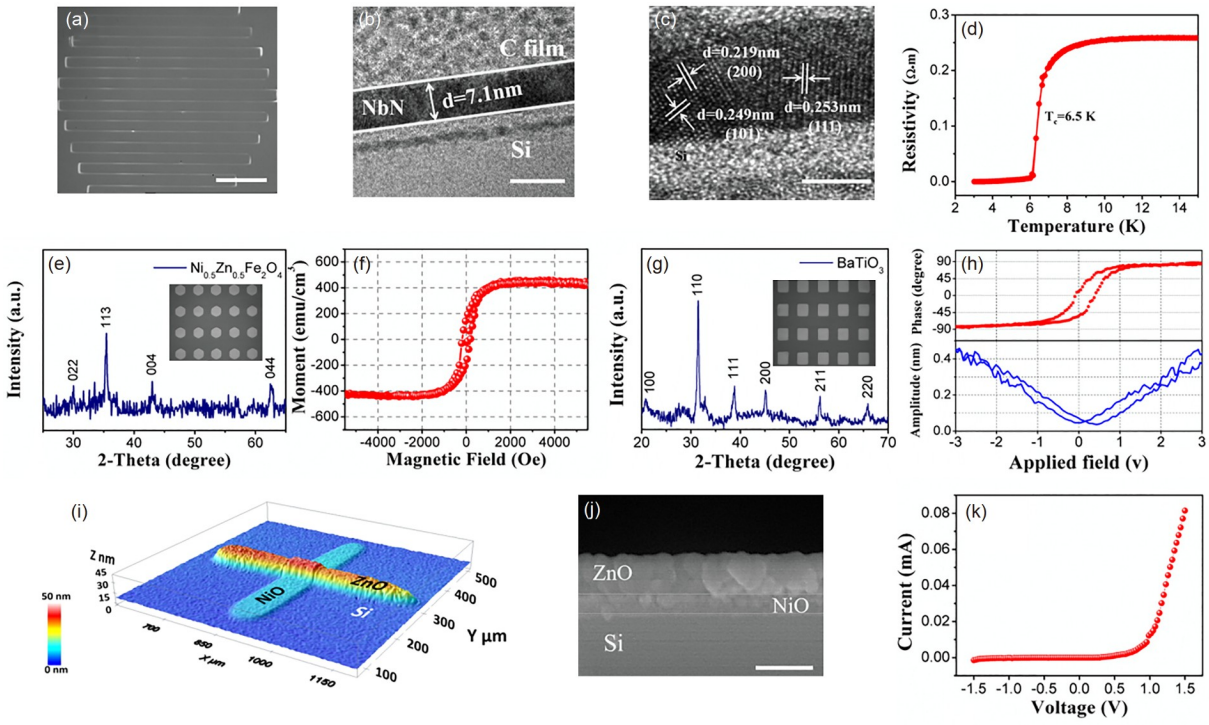

Figure 5 Laser-printed NbN superconductor microwires and ZnO/NiO transistor. (a) SEM image of the printed circuitous NbN microwire on Si substrate (scale bar = 50 μm); (b) cross-section TEM image of the printed NbN (scale bar = 10 nm); (c) HRTEM of the NbN (scale bar = 5 nm); (d) temperature dependent resistivity of the NbN film; (e) XRD spectra of the printed Ni-Zn ferrite (inset shows the optical image of the printed pattern); (f) magnetization of the printed Ni-Zn ferrite; (g) XRD spectrum of the printed $BaTiO_3$ (inset shows the optical image of the printed pattern); (h) polarizing phase and strain amplitude hysteresis loop of the printed $BaTiO_3$ from PFM test; (i) 3D image of the ZnO-NiO heterojunction; (j) cross-section SEM image of the ZnO-NiO heterojunction (scale bar = 50 nm); (k) *I-V* characteristic of the ZnO-NiO heterojunction (color online).

(HRTEM) image clearly reveals the NbN (111), (101), and (200) lattice planes, indicating that the printed NbN is highly crystallized and with a polycrystalline morphology (Figure 5c). The temperature-dependent resistivity of the printed NbN was tested (Figure 5d). The NbN resistivity decreased to 0 Ohm at 6.5 K, which corresponds to a superconducting transition temperature (T_c). The T_c is comparable to the critical temperature of the NbN grown by physical deposition methods [48]. A printed Ni-Zn ferrite magnetic material and a $BaTiO_3$ ferroelectric material were fabricated on Si substrates. The XRD patterns proved that these printed materials are pure phases (Figure 5e–g). Both the magnetization (Figure 5f) and the piezo-response force microscopy (Figure 5h, Figure S8) responses are comparable with those of the bulk materials [49,50]. In addition to the simple patterning of thin films, we also performed layer-by-layer printing, which allows the additive construction of multiple components forming heterostructures and electronic devices. Figure 5i shows a printed transistor of p-type NiO and n-type ZnO through a layer-by-layer fabrication. The cross-section scanning electron microscopy (SEM) image shows that both NiO and ZnO layers are dense and uniform (Figure 5j) and that the interface between the two layers is seamless. The printed heterojunction shows the typical current-voltage (*I-V*) characteristic of a diode that is conductive at positive bias and rectifying (high resistance) at negative bias voltage (Figure 5k).

The latest reports on the laser additive manufacturing of inorganics have achieved high resolutions for 3D nanostructures. Šakirzanovas *et al*. [51] utilized photoactive preceramic polymers as precursor, achieving a new resolution record below 60 nm in the laser printing of Si/ZrO_2 3D nanostructures. Vyatskikh *et al*. [8] applied a preceramic TiO_2 resist as precursor to fabricate high-refractive-index TiO_2 3D architectures with 300–600 nm beam dimensions. Gonzalez-Hernandez *et al*. [52] applied ultrafast laser direct-write (LDW) nanolithography for printing inorganic free-form micro-optics. However, a high flexibility allowing printing of a greater variety of inorganics and enriching their functional properties had not yet been achieved. This work demonstrates the SLL printing of a variety of inorganics with ferroelectric, magnetic, semiconductivity, and superconductivity properties, opening up more opportunities for expanding the applications of laser additive manufacturing. Although the best resolution achieved in this work, which is limited by our commercial NIR laser direct writing equipment, was not less than 10 μm, it should be possible to further reduce the feature size to the submicrometer range by optimizing the laser beam, increasing the objective lens numerical aperture, performing immersion exposure, or other

methods. For example, Ko *et al*. [53,54] have achieved a 380 nm metal wire by direct writing through the application of a 780 nm wavelength femtosecond laser. Vyatskikh *et al*. [7] have reported a 100-nm resolution utilizing a two-photo lithography laser printing system. Besides laser direct writing, the resolution may also be improved by the use of emerging nanotechnologies such as dip and polymer pen lithography [55] or e-beam [56].

4 Conclusions

A brand new laser lithography strategy for carrying and printing inorganics has been developed on the basis of the Maillard reaction. Unlike the conventional photopolymerizations based on photochemical reactions of poly(vinyl cinnamates), diazido-cyclized rubbers, diazonaphthoquinone compounds, polyester derivatives, or photo acid generators of iodonium salts and sulfonium salts, the SLL method utilizes the green chemicals maltose and PEI, which are non-toxic, organic-solvent-free, environmentally friendly, and inexpensive. Most importantly, the SLL precursor is highly suitable for delivering diverse metal ions and allows printing of numerous inorganic materials comprising metals, metal oxides, metal sulfides and metal nitrides that feature ferroelectric, magnetic, semiconductivity, superconductivity or other properties. These printed functional materials and electronic devices show quality and physical properties comparable to those of solution-processed bulk materials. In addition, the SLL precursor is uniform, stable, supports metal ion mixtures, and allows printing of polymetallic compounds. A maximum laser scanning speed of 1,500 mm/s has been demonstrated and the microstructures can be easily scaled up to the centimetre range, providing a firm basis for applications. This new lithography manufacturing method opens up a new avenue for printing functional inorganic materials and devices, and expedites potential applications of structure dependent electronic, optical, chemical, and biological systems.

Acknowledgements This work was supported by the National Natural Science Foundation of China (21971172, 21671141, and 21601130) and the Priority Academic Program Development (PAPD) of Jiangsu Higher Education Institutions for Optical Engineering in Soochow University.

Conflict of interest The authors declare no conflict of interest.

Supporting information The supporting information is available online at http://chem.scichina.com and http://link.springer.com/journal/11426. The supporting materials are published as submitted, without typesetting or editing. The responsibility for scientific accuracy and content remains entirely with the authors.

1 Li J, Pumera M. *Chem Soc Rev*, 2021, 50: 2794–2838
2 Pan JA, Rong Z, Wang Y, Cho H, Coropceanu I, Wu H, Talapin DV. *J Am Chem Soc*, 2021, 143: 2372–2383
3 Cui H, Hensleigh R, Yao D, Maurya D, Kumar P, Kang MG, Priya S, Zheng XR. *Nat Mater*, 2019, 18: 234–241
4 Capel AJ, Rimington RP, Lewis MP, Christie SDR. *Nat Rev Chem*, 2018, 2: 422–436
5 Blasco E, Müller J, Müller P, Trouillet V, Schön M, Scherer T, Barner-Kowollik C, Wegener M. *Adv Mater*, 2016, 28: 3592–3595
6 Shukla S, Vidal X, Furlani EP, Swihart MT, Kim KT, Yoon YK, Urbas A, Prasad PN. *ACS Nano*, 2011, 5: 1947–1957
7 Vyatskikh A, Delalande S, Kudo A, Zhang X, Portela CM, Greer JR. *Nat Commun*, 2018, 9: 593
8 Vyatskikh A, Ng RC, Edwards B, Briggs RM, Greer JR. *Nano Lett*, 2020, 20: 3513–3520
9 Eckel ZC, Zhou C, Martin JH, Jacobsen AJ, Carter WB, Schaedler TA. *Science*, 2016, 351: 58–62
10 Wang X, Schmidt F, Hanaor D, Kamm PH, Li S, Gurlo A. *Addit Manuf*, 2019, 27: 80–90
11 Kotz F, Arnold K, Bauer W, Schild D, Keller N, Sachsenheimer K, Nargang TM, Richter C, Helmer D, Rapp BE. *Nature*, 2017, 544: 337–339
12 Zeng Y, Yan Y, Yan H, Liu C, Li P, Dong P, Zhao Y, Chen J. *J Mater Sci*, 2018, 53: 6291–6301
13 He R, Liu W, Wu Z, An D, Huang M, Wu H, Jiang Q, Ji X, Wu S, Xie Z. *Ceram Int*, 2018, 44: 3412–3416
14 Hildebrand G, Sänger JC, Schirmer U, Mantei W, Dupuis Y, Houbertz R, Liefeith K. *Ceramics*, 2021, 4: 224–239
15 Sun YL, Li Q, Sun SM, Huang JC, Zheng BY, Chen QD, Shao ZZ, Sun HB. *Nat Commun*, 2015, 6: 8612
16 Wang Y, Fedin I, Zhang H, Talapin DV. *Science*, 2017, 357: 385–388
17 Yee DW, Lifson ML, Edwards BW, Greer JR. *Adv Mater*, 2019, 31: 1901345
18 Chung J, Bieri NR, Ko S, Grigoropoulos CP, Poulikakos D. *Appl Phys A*, 2004, 79: 1259–1261
19 Ko SH, Pan H, Grigoropoulos CP, Luscombe CK, Fréchet JMJ, Poulikakos D. *Nanotechnology*, 2007, 18: 345202
20 Pan H, Hwang DJ, Ko SH, Clem TA, Fréchet JMJ, Bäuerle D, Grigoropoulos CP. *Small*, 2010, 6: 1812–1821
21 Hong S, Yeo J, Kim G, Kim D, Lee H, Kwon J, Lee H, Lee P, Ko SH. *ACS Nano*, 2013, 7: 5024–5031
22 Kim KK, Ha IH, Kim M, Choi J, Won P, Jo S, Ko SH. *Nat Commun*, 2020, 11: 2149
23 Jung J, Cho H, Choi SH, Kim D, Kwon J, Shin J, Hong S, Kim H, Yoon Y, Lee J, Lee D, Suh YD, Ko SH. *ACS Appl Mater Interfaces*, 2019, 11: 15773–15780
24 Kwon J, Cho H, Suh YD, Lee J, Lee H, Jung J, Kim D, Lee D, Hong S, Ko SH. *Adv Mater Technol*, 2016, 2: 1600222
25 Nam VB, Shin J, Choi A, Choi H, Ko SH, Lee D. *J Mater Chem C*, 2021, 9: 5652–5661
26 Shin J, Jeong B, Kim J, Nam VB, Yoon Y, Jung J, Hong S, Lee H, Eom H, Yeo J, Choi J, Lee D, Ko SH. *Adv Mater*, 2020, 32: 1905527
27 Nam VB, Shin J, Yoon Y, Giang TT, Kwon J, Suh YD, Yeo J, Hong S, Ko SH, Lee D. *Adv Funct Mater*, 2019, 29: 1806895
28 Stadler RH, Blank I, Varga N, Robert F, Hau J, Guy PA, Robert MC, Riediker S. *Nature*, 2002, 419: 449–450
29 Thorpe SR, Baynes JW. *Amino Acids*, 2003, 25: 275–281
30 Ajandouz EH, Tchiakpe LS, Ore FD, Benajiba A, Puigserver A. *J Food Sci*, 2001, 66: 926–931
31 Friedman M. Lysinoalanine formation in soybean proteins: kinetics and mechanisms. In: Cherry JP, Ed. *Food Protein Deterioration*. Vol. 206. Chapter 10. Washington: American Chemical Society, 1982. 231–273
32 Finot PA, Bujard E, Mottu F, Mauron J. Availability of the true Schiff's bases of lysine. Chemical evaluation of the Schiff's base between lysine and lactose in milk. In: Friedman M, Ed. *Protein Crosslinking. Advances in Experimental Medicine and Biology*. Vol 86. Boston: Springer. 1977. 343–365
33 Kobayashi S, Hiroishi K, Tokunoh M, Saegusa T. *Macromolecules*,

1987, 20: 1496–1500
34 Zou GF, Zhao J, Luo HM, McCleskey TM, Burrell AK, Jia QX. *Chem Soc Rev*, 2013, 42: 439–449
35 Skliutas E, Lebedevaite M, Kabouraki E, Baldacchini T, Ostrauskaite J, Vamvakaki M, Farsari M, Juodkazis S, Malinauskas M. *Nanophotonics*, 2021, 10: 1211–1242
36 Jansen RJJ, van Bekkum H. *Carbon*, 1995, 33: 1021–1027
37 Martins SIFS, Jongen WMF, van Boekel MAJS. *Trends Food Sci Tech*, 2000, 11: 364–373
38 O'Neill W, Kun Li W. *IEEE J Sel Top Quantum Electron*, 2009, 15: 462–470
39 Hsiao WT, Tseng SF, Huang KC, Wang YH, Chen MF. *Int J Adv Manuf Technol*, 2011, 56: 223–231
40 Aydinli A, Lo HW, Lee MC, Compaan A. *Phys Rev Lett*, 1981, 46: 1640–1643
41 Arca E, Fleischer K, Shvets IV. *J Phys Chem C*, 2009, 113: 21074–21081
42 Bandara J, Divarathne CM, Nanayakkara SD. *Sol Energy Mater Sol Cells*, 2004, 81: 429–437
43 Luo H, Lin Y, Wang H, Chou CY, Suvorova NA, Hawley ME, Mueller AH, Ronning F, Bauer E, Burrell AK, McCleskey TM, Jia QX. *J Phys Chem C*, 2008, 112: 20535–20538
44 Baker MA, Greaves SJ, Wendler E, Fox V. *Thin Solid Films*, 2000, 377-378: 473–477
45 Li H, Zhang Q, Yap CCR, Tay BK, Edwin THT, Olivier A, Baillargeat D. *Adv Funct Mater*, 2012, 22: 1385–1390
46 Tan JMR, Lee YH, Pedireddy S, Baikie T, Ling XY, Wong LH. *J Am Chem Soc*, 2014, 136: 6684–6692
47 Yi Q, Wu J, Zhao J, Wang H, Hu J, Dai X, Zou G. *ACS Appl Mater Interfaces*, 2017, 9: 1602–1608
48 Kang L, Jin BB, Liu XY, Jia XQ, Chen J, Ji ZM, Xu WW, Wu PH, Mi SB, Pimenov A, Wu YJ, Wang BG. *J Appl Phys*, 2011, 109: 033908
49 Costa ACFM, Tortella E, Morelli MR, Kiminami RHGA. *J Magn Magn Mater*, 2003, 256: 174–182
50 Mao HJ, Song C, Xiao LR, Gao S, Cui B, Peng JJ, Li F, Pan F. *Phys Chem Chem Phys*, 2015, 17: 10146–10150
51 Merkininkaitė G, Aleksandravičius E, Malinauskas M, Gailevičius D, Šakirzanovas S. *Opto-Electron Adv*, 2022, 5: 210077
52 Gonzalez-Hernandez D, Varapnickas S, Merkininkaitė G, Čiburys A, Gailevičius D, Šakirzanovas S, Juodkazis S, Malinauskas M. *Photonics*, 2021, 8: 577
53 Son Y, Yeo J, Moon H, Lim TW, Hong S, Nam KH, Yoo S, Grigoropoulos CP, Yang DY, Ko SH. *Adv Mater*, 2011, 23: 3176–3181
54 Hong S, Lee H, Yeo J, Ko SH. *Nano Today*, 2016, 11: 547–564
55 Huo F, Zheng Z, Zheng G, Giam LR, Zhang H, Mirkin CA. *Science*, 2008, 321: 1658–1660
56 Chen Y. *Microelectron Eng*, 2015, 135: 57–72